

Quantum spin liquid with emergent chiral order in the triangular-lattice Hubbard model

Bin-Bin Chen^{1,2,3}, Ziyu Chen¹, Shou-Shu Gong^{1,*}, D. N. Sheng⁴, Wei Li^{5,1,†} and Andreas Weichselbaum^{6,2,‡}

¹*School of Physics, Beihang University, Beijing 100191, China*


²*Arnold Sommerfeld Center for Theoretical Physics, Center for NanoScience, and Munich Center for Quantum Science and Technology, Ludwig-Maximilians-Universität München, 80333 Munich, Germany*

³*Department of Physics and HKU-UCAS Joint Institute of Theoretical and Computational Physics, The University of Hong Kong, Pokfulam Road, Hong Kong SAR, China*

⁴*Department of Physics and Astronomy, California State University, Northridge, California 91330, USA*

⁵*CAS Key Laboratory of Theoretical Physics, Institute of Theoretical Physics, Chinese Academy of Sciences, Beijing 100190, China*

⁶*Department of Condensed Matter Physics and Materials Science, Brookhaven National Laboratory, Upton, New York 11973-5000, USA*

 (Received 19 February 2021; revised 30 June 2022; accepted 31 August 2022; published 16 September 2022)

The interplay between spin frustration and charge fluctuation gives rise to an exotic quantum state in the intermediate-interaction regime of the half-filled triangular-lattice Hubbard model, while the nature of the state is under debate. Using the density matrix renormalization group with $SU(2)_{\text{spin}} \otimes U(1)_{\text{charge}}$ symmetries implemented, we study the triangular-lattice Hubbard model defined on the long cylinder geometry up to circumference $W = 6$. A gapped quantum spin liquid, with on-site interaction $9 \lesssim U/t \lesssim 10.75$, is identified between the metallic and the antiferromagnetic Mott insulating phases. In particular, we find that this spin liquid develops a robust long-range spin scalar-chiral correlation as the system length L increases, which unambiguously unveils the spontaneous time-reversal symmetry breaking. In addition, the degeneracy of the entanglement spectrum supports symmetry fractionalization and spinon edge modes in the obtained ground state. The possible origin of chiral order in this intermediate spin liquid and its relation to the rotonlike excitations have also been discussed.

DOI: [10.1103/PhysRevB.106.094420](https://doi.org/10.1103/PhysRevB.106.094420)

I. INTRODUCTION

Since Anderson's seminal work on the resonating valence bond (RVB) state in quantum antiferromagnets [1,2], searching for spin-liquid states and the consequent superconductivity after doping constitutes an exciting topic in condensed-matter physics [3]. While it has been widely accepted that spin frustration plays the key role for the emergence of spin liquid in Mott insulators [4–6], it has also been noticed that the strong charge fluctuations near the Mott transition may add an additional active ingredient to the system [7,8]. Although stable spin-liquid states in the half-filled bipartite-lattice Hubbard models have not been established [9], the frustrated triangular-lattice Hubbard (TLU) model, harboring stronger spin and charge fluctuations at intermediate Hubbard interaction U , has raised great interest in the possible intermediate spin-liquid state [10–16].

Meanwhile, experimental progress in the triangular-lattice organic-salt compounds κ -(BEDT-TTF)₂Cu₂(CN)₃ [17–22] and EtMe₃Sb[Pd(dmit)₂]₂ [23,24] also shed light on the spin-liquid states near the Mott transition. The absence of spin ordering down to the lowest experimental temperature and the linear- T dependence of low-temperature specific heat suggest a possible gapless spin liquid in these compounds [19,24].

However, recent thermal conductivity measurements indicate the absence of mobile gapless excitations [25,26]. The experimental identification of the spin liquid and the pursuit of its nature have further stimulated intensive theoretical studies.

To include the charge fluctuation effects, one can consider the higher-order ring-exchange coupling in the effective spin model [7,27–30] or simulate the Hubbard model directly. Indeed, numerical simulations on the ring-exchange spin model have identified a gapless spin-liquid state with the emergent spinon Fermi surface [7,28,31], which can partly explain the experimental findings. On the other hand, large-scale density matrix renormalization group (DMRG) simulations on the TLU itself have uncovered a spin-liquid phase near the Mott transition [14,15]. However, the two different studies lead to drastically distinct conclusions on the nature of this spin liquid. While the finite-DMRG calculation [14] suggests a Dirac-like gapless spin liquid preserving time-reversal symmetry (TRS), the more extensive infinite-DMRG study [15] finds a gapped chiral spin liquid (CSL) with finite chiral order [32–35]. Moreover, the spinon Fermi-surface state is not found in these DMRG simulations, in contrast to the previous understanding based on the effective spin model.

In this work, we further determine the precise nature of the spin liquid phase in the TLU. After introducing the model and method in Sec. II, we perform extensive DMRG calculations on finite-size cylinders for a fixed width $W = 4$ (YC4; cf. Fig. 1) in Sec. III, where we gradually increase the system length up to $L = 64$. This goes far beyond the previous finite-size DMRG [14] and thus significantly reduces finite-size

* shoushu.gong@buaa.edu.cn

† w.li@itp.ac.cn

‡ weichselbaum@bnl.gov

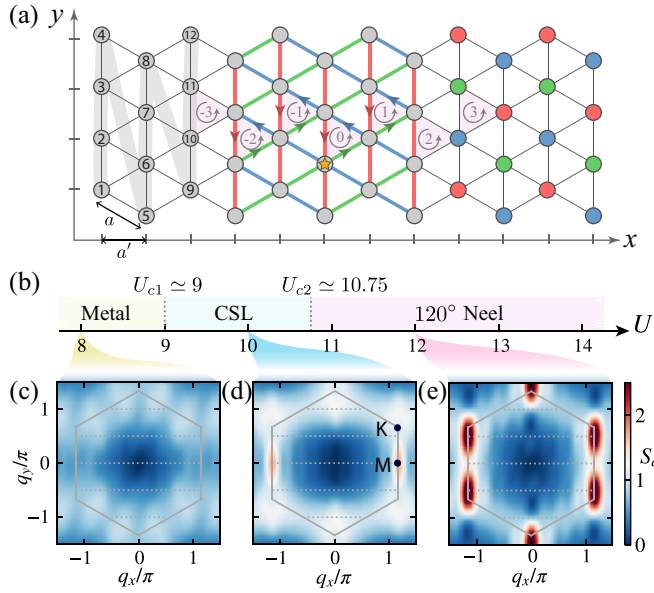


FIG. 1. Model and phase diagram. (a) Triangular-lattice cylinder with open (periodic) boundary conditions along the x (y) direction and lattice spacing $a = 1$. Having a straight open edge, i.e., YC4 geometry, the columnar spacing is $a' = \sqrt{3}/2$. (For later reference, an XC geometry has straight horizontal chains at distance a' with a zigzag open boundary left and right.) The DMRG simulations employ a 1D “zigzag” mapping as indicated by the gray-shaded path (with part of the site ordering also indicated). The yellow star denotes the central reference site for which the spin-spin correlation is calculated, while the pink triangles for evaluating the chiral correlations are ordered symmetrically away from the center. The arrows on the bonds denote the current directions of the chiral order, having three colors for the three different directions. (b) The phase diagram of the TLU model consists of a metallic phase, a fully gapped CSL phase, and a 120° spin-ordered phase, with the three colors of the sites denoting the three-sublattice structure. (c)–(e) Typical static spin structure factors S_q for $U = 8, 10$, and 12 in the three phases.

effects, which is followed by an analysis of width $W = 6$ cylinders (YC6) in Sec. III E, with strong evidence also for a chiral phase there, albeit with slightly altered phase boundaries. Throughout, we emphasize the necessity to exploit the $SU(2)_{\text{spin}} \otimes U(1)_{\text{charge}}$ symmetries in our DMRG simulation, as this permits us to reliably reach large-scale systems. We identify an intermediate nonmagnetic phase with ultrashort single-particle and spin correlation lengths on the order of one lattice spacing, having $(U_{c1} \simeq 9t) \lesssim U \lesssim (U_{c2} \simeq 10.75t)$ for $W = 4$. On short cylinders we find exponentially decaying chiral correlation in agreement with Ref. [14], but the result changes fundamentally with increasing system length, showing very robust long-range chiral correlation characterizing spontaneous TRS breaking. We also find a large degeneracy in the entanglement spectrum, which agrees with symmetry fractionalization and the existence of an edge spinon in the obtained ground state. Therefore, we conclude that the low-energy physics of the TLU model at the intermediate- U is governed by a gapped CSL. Our results show the importance of a sufficiently large system length to overcome finite-size effects for identifying TRS breaking in this system. In the

outlook in Sec. IV, we point out a possible link between the present results and the chiral nature of excitations found in the triangular lattice Heisenberg (TLH) model at finite temperature [36].

II. MODEL AND METHOD

The TLU model is defined as

$$\hat{\mathcal{H}} = -t \sum_{\langle i,j \rangle, \sigma} (\hat{c}_{i\sigma}^\dagger \hat{c}_{j\sigma} + \text{H.c.}) + \frac{U}{2} (\hat{n}_i - 1)^2, \quad (1)$$

where $\langle \cdot, \cdot \rangle$ represents the summation over the nearest-neighbor (NN) couplings, $\hat{c}_{i\sigma}$ ($\hat{c}_{i\sigma}^\dagger$) denotes the fermionic annihilation (creation) operator with spin $\sigma \in \{\uparrow, \downarrow\}$ on site i , and $\hat{n}_i = \sum_{\sigma} \hat{n}_{i\sigma}$, with $\hat{n}_{i\sigma} \equiv \hat{c}_{i\sigma}^\dagger \hat{c}_{i\sigma}$ the particle number operator. We set $t := 1$ as the unit of energy, and the unit of distance via the lattice spacing $a := 1$, throughout. In our DMRG calculations [37], we mainly focus on YC4 cylinders as shown in Fig. 1(a), but we also extend to XC4 and YC6 cylinders. Throughout, we implement the $SU(2)_{\text{spin}} \otimes U(1)_{\text{charge}}$ symmetries based on the QSpace tensor library [38,39], which enables us to retain up to $D^* = 8192$ multiplets [equivalent to about $D \sim 24\,000$ $U(1)$ states] and ensures full convergence with a truncation error $\lesssim 1 \times 10^{-6}$.

III. WIDTH 4 CYLINDERS (YC4)

A. Ground-state phase diagram

We summarize our DMRG phase diagram in Fig. 1(b) with a metallic phase for $U < U_{c1} (\simeq 9)$, a 120° magnetically coplanar-ordered phase [40–42] for $U > U_{c2} (\simeq 10.75)$, and an intermediate CSL phase with spontaneous TRS breaking. Figures 1(c)–1(e) show the representative snapshots of the static spin structure factors $S_q \equiv \sum_j e^{iq \cdot R_{0j}} \langle \hat{S}_j \cdot \hat{S}_0 \rangle$ in the different phases, where site 0 refers to a fixed site in the center of the system [cf., the asterisk site in Fig. 1(a)]. In the metallic phase (small U), S_q is found to be featureless. In the CSL phase [Fig. 1(d)], a peak emerges at the M point which is related to short-range stripe correlation. Further increasing U , sharp peaks emerge around the K points [Fig. 1(e)], consistent with a semiclassical 120° spin order. Even though the present YC4 geometry is not fully compatible with the 120° order, the feature of the dominant K point peak can still be observed. For very large $U \gtrsim 20$, eventually, the ground state on the particular YC4 cylinder switches to an RVB ringlike state [43], which is beyond the scope of interest here.

The phase boundaries of the CSL phase are estimated in Fig. 2. By contrasting the U dependence of S_q at $q = K$ with M in Fig. 2(a) [44], strongly enhanced magnetic correlations at the M points appear in the intermediate regime, up to $L = 64$. For $L = 18$, this leads to two crossing points of S_M with S_K . We use the upper crossing to estimate the phase boundary towards the 120° order, resulting in $U_{c2} \simeq 10.75$. The lower phase boundary towards the metallic phase represents a metal-insulator transition that is more naturally characterized by an analysis of the double occupancy $n_d \equiv \langle \psi | \hat{n}_{0\uparrow} \hat{n}_{0\downarrow} | \psi \rangle$, which is related to local charge or energy fluctuations of a single site (computed at the central site $i = 0$ here). Starting from half-filling, this expectation value acquires a finite value for $U \gg t$ via a second-order process. In the infinite- U

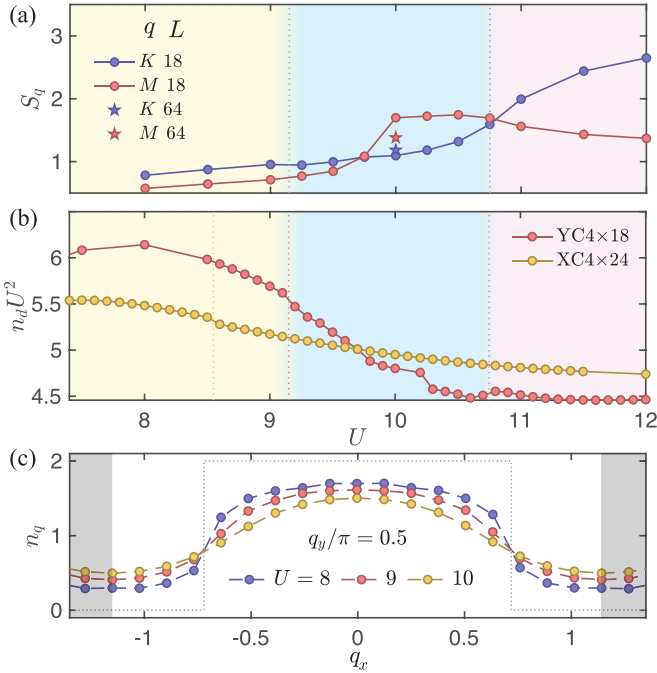


FIG. 2. Hubbard U dependence of different quantities on the YC4 \times L cylinders. (a) Spin structure factors S_q at the K and M points. The $L = 64$ data are also shown at $U = 10$. The asterisks show data points for the significantly longer system that exhibits long-range chiral correlations as analyzed in Fig. 4. (b) Double occupancy shown as $n_d U^2$. This also includes XC4 data, which exhibit only one discontinuity around the metal-insulator transition. (c) Distribution of n_q vs q_x in the momentum space along $q_y = \pi/2$. The dashed line plots n_q for $U = 0$ on the torus system with the same size 4×18 . The white center region marks the first Brillouin zone.

limit, one can thus estimate for the magnetically completely uncorrelated case $n_d \simeq \frac{z^2}{2U^2}$, with z the coordination number. Antiferromagnetic correlations tend to increase this value. Also as U is lowered, charge fluctuations generally increase via higher-order processes. Hence in the present case with $z = 6$ and $t = 1$, we can consider $n_d U^2 \gtrsim 3$ a lower bound. Also from a numerical perspective with $U \sim 10$, we have for the double occupancy $n_d \ll 1$, such that accurate numerical simulations are important. Now when plotting $n_d U^2$ versus U for the YC4 system [Fig. 2(b)], we observe the onset of a kink around $U \simeq 9$, which we thus interpret as the lower phase boundary U_{c1} . Note, however, that this value for U_{c1} does not coincide with the lower crossing of S_M versus S_K in Fig. 2(a), which may be due to the finite-size effects, considering that the lower phase boundary is significantly more demanding numerically given that both spin and charge gaps close there. For YC4, the double occupancy $n_d U^2$ shows another discontinuity around the magnetic transition U_{c2} , and it stays rather constant thereafter. For comparison, we also include data for the XC4 geometry in Fig. 2(b). In contrast to YC4, this only exhibits one discontinuity around U_{c1} . Overall, it is smoother, varies significantly less versus U , and remains higher for the largest U . Together with the fact that 120° order is commensurate with XC4, we take the above finding as an indication that the intermediate chiral phase is absent for the XC4 geometry. As such, it exhibits a lesser degree of frustration and favors the

large- U magnetic correlations already at smaller U . As an aside, we note that the interpretation that frustration is less pronounced for XC4 is also supported by Ref. [42], where no dimerization was observed in the Heisenberg limit.

The metal-insulator transition also manifests itself in the change of the Fermi surface with increasing U . For this, we analyze the one-particle charge density in momentum space, $n_q \equiv \sum_{\sigma} \sum_j e^{iq \cdot R_{0j}} \langle \hat{c}_{j\sigma}^\dagger \hat{c}_{0\sigma} \rangle$ in Fig. 2(c). At $U = 0$, n_q is a steplike function (dashed line). With increasing U , the drop of n_q is gradually smoothed until the Fermi surface disappears [15]. To be specific, within the resolution for $L = 18$, n_q at $U = 8$ still exhibits an appreciable “jump” at $q_x \simeq \pm 3\pi/4$ with fixed $q_y = \pi/2$. However, for $U \gtrsim 9$, n_q changes smoothly and the Fermi surface appears to be absent (cf. Appendix D), indicating a metal-insulator transition. Our estimates of the phase boundaries are roughly consistent with those reported in previous studies [13–15, 29, 45]. Minor quantitative deviation of the lower boundary U_{c1} is likely due to the different geometry and system size.

B. Fully gapped spin liquid

Next we focus on the charge and spin excitations in the spin-liquid phase. In Fig. 3(a), the single-particle Green’s function $\langle \hat{c}_i^\dagger \hat{c}_j \rangle$, averaged among all site pairs with the same distance d_{ij} , decays exponentially versus d_{ij} with a short correlation length $\xi_c \simeq 0.81$. This is consistent with a sizable charge (single-particle excitation) gap $\Delta_c \simeq 0.88$ extrapolated for $1/L \rightarrow 0$ (see Appendix G) and verifies that the spin liquid resides in the Mott insulator phase.

In Fig. 3(b), we show the spin correlation $\langle \hat{S}_i \cdot \hat{S}_j \rangle$ versus d_{ij} , which is well converged and clearly decays exponentially, with a short correlation length $\xi_s \simeq 1.66$. Such a short correlation length implies gapped spin excitations, which do not support a spinon Fermi surface state with algebraically decaying spin correlation [7] but could be consistent with either a gapped spin liquid or a Dirac-like gapless spin liquid that is gapped due to finite size on narrow-width cylinders. As shown in Fig. 3(c), this conclusion is further supported by the saturated bipartite entanglement entropy S_E vs subblock size l_x , following an area law [46].

By analyzing the convergence of the DMRG simulation with increasing D^* (see Appendices B and G for details), we find that the chiral correlations become well-established only once the accuracy of the energy per site reaches a resolution of $\Delta e_\chi \cong e_g - e_g^0 \simeq 10^{-3}$ for YC4 \times 64 [e.g., see Fig. 9(h)], where the kink in the convergence of the ground-state energy around $1/D^* \sim 5 \times 10^{-4}$ with $\delta e_g \simeq 10^{-3}$ relates to a significant buildup of entanglement entropy in Fig. 9(g) still, before it converges to a plateau]. Based on this, one may estimate a sizable bulk gap $\Delta_\chi \simeq N \Delta e_\chi \sim 0.26$ with the chiral phase, with $N \equiv L W$ the total number of sites. Nevertheless, since large system sizes are required to capture the chiral phase, the bulk gap’s relative effect on the ground-state energy is very small, thus requiring an energy accuracy of at least 0.2% for the case of YC4 \times 64. Therefore, sufficiently accurate simulations on large systems are important. In the present case, this is made possible by fully exploiting the SU(2) spin symmetry. The sizable bulk gap Δ_χ is consistent with the extremely short spin and charge correlation lengths on the order of the lattice

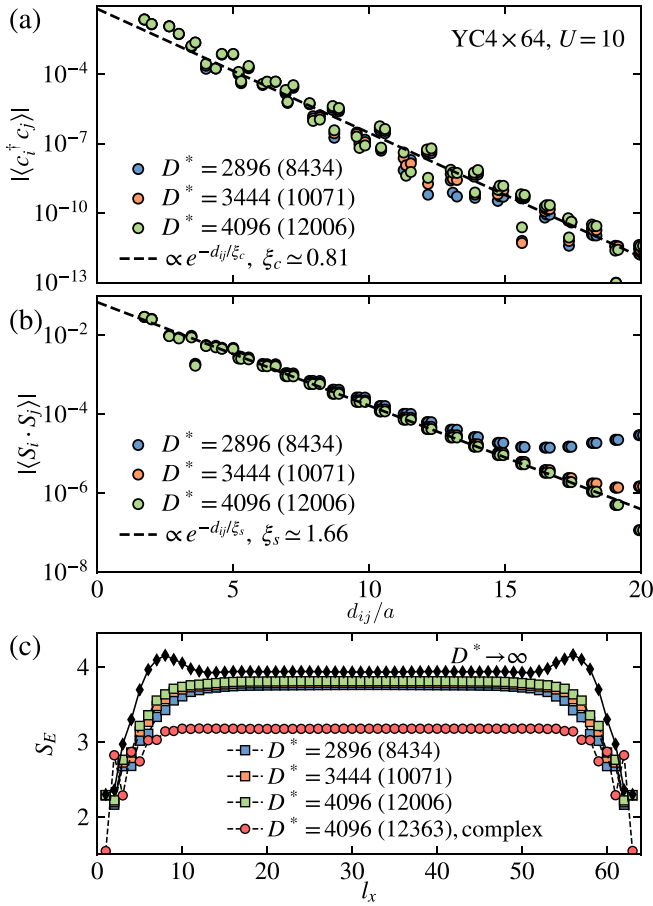


FIG. 3. Single-particle Green's function, spin correlation, and entanglement entropy obtained on the YC4 \times 64 cylinder at $U = 10$. Log-linear plot of (a) single-particle Green's function $|\langle c_i^\dagger c_j \rangle|$, and (b) spin correlation $|(S_i \cdot S_j)|$ as a function of distance d_{ij} , which show exponential decay with short decay lengths $\xi_c \simeq 0.81$ and $\xi_s \simeq 1.66$, respectively. (c) Bipartite entanglement entropy $S_E = -\sum_i \rho_i \ln \rho_i$ for the reduced density matrix ρ when cutting the system at bond l_x vs. block size l_x . This shows a well-developed plateau for $12 \leq l_x \leq 52$, and hence obeys the area law in the bulk. We include a linear extrapolation $1/D^* \rightarrow 0$ (black symbols). S_E is also obtained from a complex wave function (red symbols; all other data for a real wave function) with the value of the plateau in the center reduced by $\ln(2 \pm 0.1)$.

spacings itself, as seen in Fig. 3. Importantly, these correlation lengths are already also much shorter than the width of the YC4 cylinder analyzed here. In this sense, it appears plausible that the chiral phase persists to wider systems in the low-energy regime. And, indeed, as we will demonstrate further below, we see a consistent picture including chiral long-range correlations also for the YC6 cylinder.

C. Spontaneous time-reversal symmetry breaking

One key debate in the previous DMRG studies is whether there exists a spontaneous TRS breaking [15] or not [14]. Here we resolve this issue by calculating the spin chiral correlation $\langle \hat{\chi}_i \hat{\chi}_j \rangle$ (see the Appendixes for more details) between two three-spin triangles Δ_i and Δ_j symmetrically separated from the system center, i.e., having $i = -j$ or $i = 1 - j$, as shown

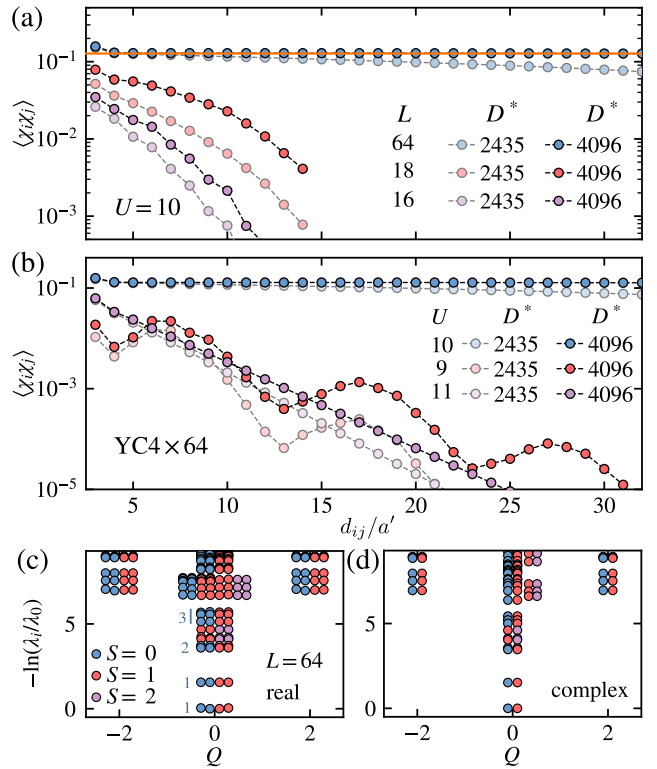


FIG. 4. Chiral correlation and entanglement spectrum of the chiral spin liquid state. (a) Chiral correlations $\langle \chi_i \chi_j \rangle$ for $U = 10$ on the YC4 cylinders with different system lengths $L = 16, 18, 64$. The orange horizontal line indicates the value of $\langle \chi_i \chi_j \rangle \simeq 0.128$ for $d_{ij} = 30$. (b) Chiral correlations for $U = 9, 10, 11$ on the YC4 \times 64 cylinder obtained by keeping the bond dimensions up to $D^* = 4096$ multiplets. Entanglement spectra of the YC4 \times 64 for both (c) real and (d) complex wave functions, grouped by charge sectors (for even Q), with spin labels color-coded as specified in the legend. The bars and respective numbers with the $Q = 0$ column in (c) indicate group degeneracy. The subtracted ground levels for the two cases are $\lambda_0 \simeq 0.08$ and $\lambda_0 \simeq 0.15$, where a relative factor of ~ 2 is observed.

in Fig. 1(a). The involved scalar chirality operator is $\hat{\chi}_i = (\hat{\sigma}_\alpha \times \hat{\sigma}_\beta) \cdot \hat{\sigma}_\gamma$, with $\alpha, \beta, \gamma \in \Delta_i$ in counterclockwise order for the Pauli operators. Given that the Hermitian operator $\hat{\chi}_i$ has purely imaginary matrix elements, using real-valued DMRG with the real-valued Hamiltonian in Eq. (1) will always yield $\langle \hat{\chi}_i \rangle = 0$. Evidently, a real-valued wave function cannot (spontaneously) break TRS. Hence we compute static chiral correlations $\langle \hat{\chi}_i \hat{\chi}_j \rangle$. Eventually, however, we do repeat precisely the same DMRG calculations but using complex arithmetic, which then permits a plain nonzero expectation value of the order parameter $\langle \hat{\chi}_i \rangle$.

We first check the system-length dependence of the chiral correlation at $U = 10$. As shown in Fig. 4(a), for small length $L = 16$ and 18 , the chiral correlations decay exponentially in the same sign, in agreement with the previous study [14]. Interestingly, by further increasing the system length, a very robust chiral correlation is established over long distances, with $\sqrt{\langle \hat{\chi}_i \hat{\chi}_j \rangle} \simeq 0.36$ for $d_{ij} = 30$ already well-converged over distance for $D^* \gtrsim 3444$ [cf. the orange horizontal guide in Fig. 4(a)]. We also perform a complex-

valued DMRG simulation in the $YC4 \times 64$ system, to directly estimate the chiral order parameter $\langle \hat{\chi} \rangle \simeq 0.35$ in the bulk, in excellent agreement with previous infinite-DMRG value $\chi_{\text{iDMRG}}(U = 10) \simeq 0.34$ [15]. Our results indicate that the system length is crucial for identifying the spontaneous TRS breaking in the DMRG calculations, which reconciles the different observations in previous studies. In Fig. 4(b) we also compute the chiral correlations in the neighboring phases. In either case, $(U = 9) \lesssim U_{c1}$ and $(U = 11) > U_{c2}$, chiral correlations decay exponentially, consistent with the preserved TRS in the two phases.

In addition, we also studied the XC cylinder, i.e., with one of the bond directions along the x -axis, with circumference up to $W = 6$. There, however, even for large L , we find no strong signature of long-range chiral correlation (see the Appendices for more details). Such different behaviors of chiral correlation on different geometries have also been observed in the DMRG study of a triangular spin model with further-neighbor interactions [35], where the chiral order on the XC cylinder emerges only at large circumference. We suspect that long-range chiral correlation ultimately also can be found on wider XC cylinder in future studies.

D. Degeneracy in the entanglement spectrum

In addition to the long-range chiral correlation, we observe systematic large degeneracy in the entanglement spectra (ES) defined by $\mathcal{E}_i \equiv -\ln(\lambda_i)$, with λ_i the Schmidt spectrum of the reduced density matrix of half the system. As shown in Fig. 4(c), the spectrum levels are grouped versus the charge quantum number Q (relative to half-filling) of the subblock, and color-coded based on the spin quantum number S . The levels are symmetric for $Q \rightarrow -Q$ because the ES are obtained in the system center. There due to the mirror symmetry, removing (adding) a particle from the left subblock necessarily adds (removes) it from the right one.

In the infinite-DMRG calculation [15], the ground state on the YC4 system is found in the semion sector of gapped CSL, where a degeneracy of 2 is observed due to the free spin- $1/2$ edge mode. Our finite-size DMRG simulations ultimately also lead to the same conclusion based on the ES structures in Figs. 4(c) and 4(d) in the chiral regime at $U = 10$. However, by comparison to Ref. [15], we find even larger ES degeneracies. In Fig. 4(c) the levels show at least an eightfold degeneracy. For example, there is systematic grouping of two singlets with two triplets (two blue and red dots, respectively). A factor 2 of this degeneracy is due to our wave function being real while the system is spontaneously TRS-broken. This yields the systematic doubling of *any* spin multiplet in Fig. 4(c), which can be precisely reduced by conducting the same simulation with complex arithmetic in Fig. 4(d). Correspondingly, an approximately $\ln(2)$ reduction of S_E is also seen in Fig. 3(c).

In addition to this twofold degeneracy, our remaining fourfold degeneracy between $S = 0$ and 1 can be understood as a consequence of the $SU(2)$ DMRG simulation on the state with $S = 1/2$ edge spinons, similar to the Haldane phase with $S = 1/2$ edge modes in the open spin-1 chain [47]. When computing the ES, we cut the system into two halves such that additional fictitious edge $S = 1/2$ degrees of freedom ap-

pear at the subblock boundary. This leads to a direct product of the $S = 1/2$ edge spinon with the fictitious $S = 1/2$, and thus it gives rise to the sum of a singlet and a triplet, i.e., $\frac{1}{2} \otimes \frac{1}{2} \equiv 0 \oplus 1$. Similarly, with a boundary $S = 3/2$ excitation, one arises at $\frac{3}{2} \otimes \frac{1}{2} \equiv 1 \oplus 2$ [red and purple dots in Figs. 4(c) and 4(d)]. The degeneracy of the ES levels agrees with the obtained ground state in the semion sector [48]. Importantly, we find that the low-lying $0 \oplus 1$ levels satisfy the $(1, 1, 2, 3, \dots)$ near-degenerate counting, which is consistent with the $SU(2)_1$ chiral conformal field theory [49] and thus provides further strong support for the gapped CSL [50].

E. Width 6 Cylinders (YC6)

In this section, we proceed to YC6 cylinders. A major incentive to look at YC6 is the fact that the 120° phase for large U fits naturally into YC6, but *not* into YC4 (for this reason, YC4 switches into an RVB-like phase for very large $U \gtrsim 20$, as already pointed out earlier [43]). As we will see, the chiral intermediate phase also persists in YC6. We take this as strong support for the existence of the intermediate CSL potentially also in the 2D thermodynamic limit. While the YC6 simulations are considerably more challenging, ultimately we encounter a rather similar and thus consistent overall picture as for YC4 [15]. Once the cylinders just become long enough, we observe clear long-range chiral correlations. Let us recall the following: the YC4 cylinders established long-range chiral correlations when (i) the cylinder was sufficiently long [which turned out to be much longer than the circumference, $L > 18$ for $W = 4$ in Fig. 4(a)], and at the same time (ii) the relative energy accuracy was clearly below 1%. Assuming that the bulk gap remains about the same, we have to aim at an even better relative energy accuracy given the increased number of sites here for $YC6 \times 64$, before one can start expecting to see long-range chiral correlations. This makes the YC6 calculations much more challenging. Yet as we show below, we succeed to demonstrate the buildup and full establishment of long-range chiral correlations also for YC6. This is in full agreement with Szasz *et al.* [15], which based on iDMRG concluded that there is also a chiral intermediate phase for YC6. However, our results are in stark contrast, e.g., to the more recent variational Monte Carlo simulations [51]. While they confirmed a chiral intermediate phase for $W = 4$, they concluded the chiral phase to be absent in the low-energy regime of $W = 6$ and thus also in the 2D limit. Similarly, the thermal simulations of Wietek *et al.* [52] argued in favor of a gapless stripy intermediate phase (or a gap too small to be detected within their DMRG-based approach of minimally entangled thermal states on YC4 cylinders). We speculate that such conclusions are related to the challenges in the DMRG simulations, as also clearly encountered here based on the requirement of large system sizes. Once under control, however, the spin bulk gap in the chiral intermediate phase is estimated to be large, i.e., of order 1 or similarly of order $J_{\text{eff}} \simeq \frac{4t^2}{U} \approx 0.44$. For reference, a finite spin-gap in the TLU at intermediate Coulomb interaction has also been reported recently in experimental studies on κ -(BEDT-TTF) $_2$ Cu $_2$ (CN) $_3$ [22].

The phase boundaries of the intermediate chiral phase can be expected to be weakly shifted for YC6 as compared to YC4. Indeed, we do not find evidence for long-range chiral

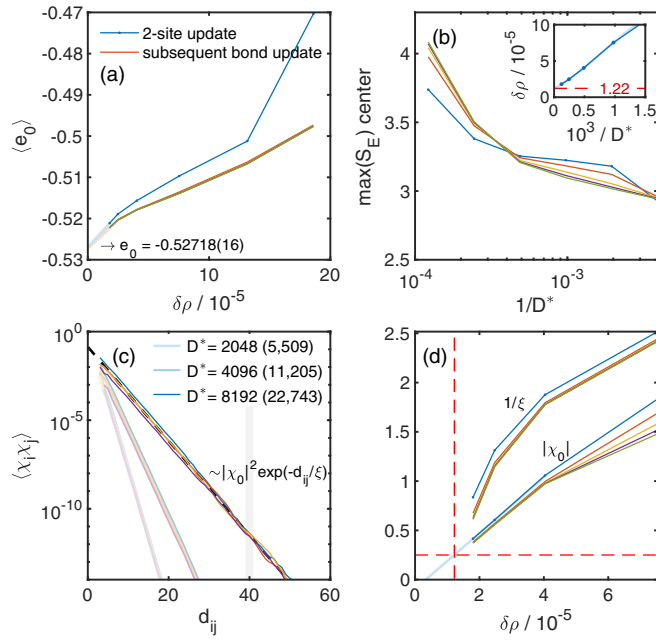


FIG. 5. DMRG simulations (real-valued) on $YC6 \times 64$ at $U = 9$. (a) Convergence of ground-state energy vs discarded weight $\delta\rho$. The lowest energies are extrapolated in a linear fashion towards $\delta\rho \rightarrow 0$, with the resulting ground-state energy per site as shown. (b) Maximum entanglement entropy around the system center vs $1/D^*$, with D^* the number of multiplets kept in the simulation. The inset shows the discarded weight vs $1/D^*$. The lines in panels (a) and (b) combine data from equivalent sweeps, such as the two-site update (line with symbol) when increasing D^* , or the subsequent four bond updates [for all other lines, see the legend to (a)]. (c) Chiral correlations vs distance. While these data show exponential decay, the correlation length is strongly dependent on D^* still. Here the various lines are derived from different combinations of up and down triangles vs distance. Different levels of color intensity refer to different D^* (D) as indicated in the legend. (d) Analysis of the parameters from the exponential fits in (c) vs discarded weight $\delta\rho$.

correlation for $U = 10$, as used for $YC4$ in Fig. 4(a). This is consistent with the analysis in [15], which also showed for $W = 6$ that the upper phase boundary for the chiral intermediate phase moves towards slightly lower values, having $U_{c2}^{YC6} \lesssim 10$ just below $U = 10$. Hence we focus on $U = 9$ for the $YC6$ system. In Fig. 5 we present a DMRG simulation on the $YC6 \times 64$ system using real-valued arithmetic. This is complemented in Fig. 6 by an identical simulation, except that it used complex-valued arithmetic, which thus permits spontaneous TRS breaking. In these simulations, for the sake of efficiency, the number D^* of kept multiplets was ramped up quickly by a factor of 2 in a two-site update, followed by four sweeps with a plain bond-update at the same D^* .

For the real-valued DMRG simulations on $YC6$ in Fig. 5, we plot the ground-state energy versus the discarded weight $\delta\rho$ in Fig. 5(a). The data converge uniformly, except that they start to show an onset towards a stronger decrease of the ground-state energy for the very smallest $\delta\rho \lesssim 2 \times 10^{-5}$. This is related to the fact that for the real-valued DMRG simulations on $YC6$ we cannot converge the chiral long-range correlations [Fig. 5(c)], despite keeping up to $D^* = 8192$ mul-

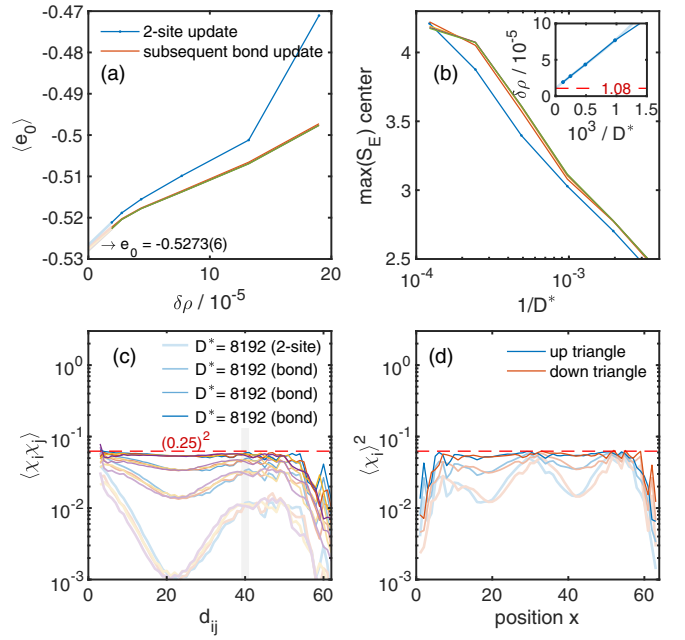


FIG. 6. DMRG simulation (complex-valued) on $YC6 \times 64$ at $U = 9$. (a)–(c) Identical analysis as in Fig. 5. (d) Having complex arithmetic, this permits a nonzero expectation value for the chiral order parameter $\langle \chi_i \rangle$, showing the square for direct comparison with (c). We note that $\langle \chi_i \rangle$ has the same sign for all triangles and, consistent with (c), converges towards $|\langle \chi \rangle| \approx 0.25$ (horizontal red dashed line). The data in (d) correspond to the last three entries in the legend in (c).

tiplets (corresponding to $D = 22\,743$ states). To be precise, while the chiral correlations in Fig. 5(c) appear to decay perfectly exponentially over long distances, the correlation length ξ is not converged in that it keeps increasing with increasing D^* , i.e., chiral correlations become stronger. The maximum entanglement entropy in the system center versus $1/D^*$ is tracked in Fig. 5(b), where its inset relates D^* to the respective discarded weight in the DMRG simulation. Since D^* is ramped up very quickly according to the DMRG sweeping protocol specified above, it looks as if $\delta\rho$ extrapolates to a finite value $\delta\rho_0 \simeq 1.22 \times 10^{-5}$ for $1/D^* \rightarrow 0$ (horizontal red dashed line). This is artificial, of course, due to the sweeping protocol, and it is attributed to the overall strong truncation still given that the system barely started to move into the low-energy chiral regime. Nevertheless, from a practical point of view, based on that inset in Fig. 5(b), computed quantities may thus be extrapolated to $\delta\rho \rightarrow \delta\rho_0 > 0$ for quantitative estimates, rather than $\delta\rho \rightarrow 0$.

The exponentially decaying chiral correlations in Fig. 5(c) were fitted by $|\chi_0|^2 e^{-d_{ij}/\xi}$. The resulting fitting parameters $|\chi_0|$ and inverse correlation length $1/\xi$ (slope) are summarized in Fig. 5(d) versus $\delta\rho$. This suggests that at the same time as $1/\xi$ extrapolates to zero at $\delta\rho \gtrsim \delta\rho_0$ [vertical red dashed line, identical to the red dashed line in the inset to Fig. 5(b)], the long-range chiral correlation assume the finite value $|\chi| \approx 0.25$ (horizontal red dashed line). Therefore, despite the fact that the real DMRG simulation cannot be converged to explicitly show long-range chiral correlations, a careful extrapolation of the data versus $\delta\rho \rightarrow 0$ (or rather

$\delta\rho \rightarrow \delta\rho_0$) does support the conclusion that the $YC6 \times 64$ cylinder based on real-valued DMRG simulations is chiral for $U = 9$.

This can be significantly more substantiated still by repeating precisely the same DMRG simulation, yet with complex arithmetic, with the results presented in Fig. 6. While the convergence of the ground-state energy in Fig. 6(a) looks nearly identical to Fig. 5(a), the maximal entanglement entropy S_E around the system center in Fig. 6(b) already starts to level off and converge for the smallest $1/D^*$ (largest $D^* = 8192$). In particular, the entanglement entropy from the two-site update (blue) remains already the same for the smallest $1/D^*$ when compared to the subsequent bond updates still (other solid lines). In Fig. 6(c), one can explicitly observe how the long-range chiral correlations build up for over the last DMRG sweeps, resulting in long-range chiral correlations of approximately $|\chi| \approx 0.25$, which is in agreement with the earlier extrapolation in Fig. 5(d). For the complex DMRG, we can also compute the chiral order parameter $|\chi|$ directly for a line of triangles along the cylinder as shown in Fig. 6(d). The data agree well in magnitude, and thus they are consistent with the chiral correlations shown in Fig. 6(c).

The nonextrapolated DMRG ground-state energy of the complex simulation ($e_0 \simeq -0.52270$) also agrees well with the real-valued calculation ($e_0 \simeq -0.52229$). The former is just slightly lower as it can explicitly make use of the TRS breaking. After simple linear extrapolation of the ground-state energies versus $\delta\rho \rightarrow 0$, one obtains $e_0 \simeq -0.5273(1)$. On a more conservative level, extrapolating $\rho \rightarrow \rho_0$ yields $e_0 \simeq -0.5245(6)$, which lowers the ground-state energy still by about 0.34%. Now given the presence of a downward kink in the convergence of the ground-state energy at the smallest energies reached, as already also seen for YC4, the subsequent extrapolated energy gain may thus again be attributed to the presence of a chiral bulk gap. Here for YC6, the estimate yields $\Delta_\chi \cong N \cdot (0.0034 e_0) \sim 0.69$, with $N = LW$ the total number of sites. The estimate for Δ_χ here for YC6 is about a factor of 2.7 larger as previously obtained in the same manner for YC4. The difference may be attributed to the slower sweeping protocol used in the DMRG for YC4, which thus underestimated the actual gap there. Importantly, in the present case the gap estimate compares well to the charge gap $\Delta_c \simeq 0.88$ explicitly evaluated for YC4 in Appendix E (cf. Fig. 12).

F. The need for long cylinders

All of the systems above required an *a priori* surprisingly large degree of asymmetry in the aspect ratio of the cylinder geometry in order to realize the intermediate phase with long-range chiral correlations. Specifically, this required the cylinders to be much longer (i.e., in the direction of the open boundary) as compared to their circumference (periodic boundary). With the notion in mind that for a topological system the bulk gap needs to close towards the boundary, the finite open boundary of the cylinders studied, in principle, can affect the cylinder considerably into the bulk itself. Naively, one may have speculated that the effects of the open edges diminish quickly as with the bulk correlation lengths for spin or charge, which, based on the data in Fig. 3 for YC4, are

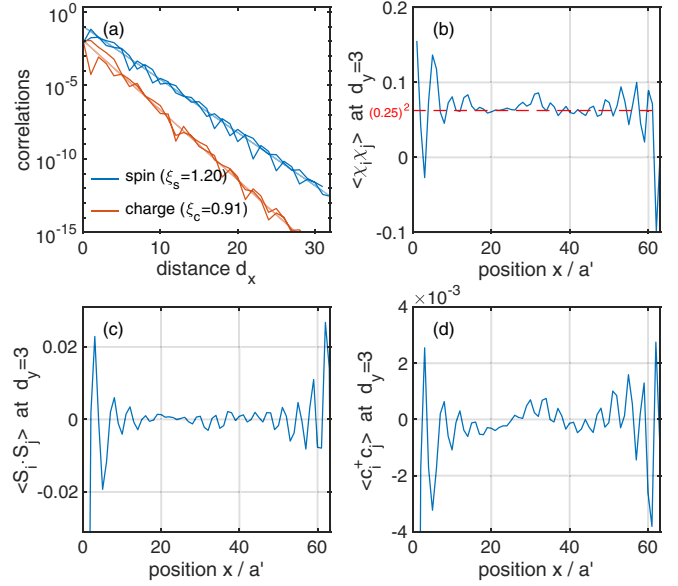


FIG. 7. Correlations in the $YC6 \times 64$ system after the last sweep in the complex DMRG simulation at $D^* = 8192$ in Fig. 6: (a) Spin $\langle S_i \cdot S_j \rangle$ and charge correlations $\langle c_i^\dagger \cdot c_j \rangle$ (where the dot product sums over spin) relative to the system center. The exponential fit $\propto e^{-x/\xi}$ (straight line in matched light color) yields the corresponding correlation length as shown with the legend. The correlations are computed along a tilted straight path of length $L - 1$ in units of lattice spacing from left to right YC boundary [cf. Fig. 1(a)]. (b) Chiral correlations, (c) spin correlations, (d) charge correlations, all at constant vertical distance $d_y = 3$ ($j = 2, 5$) vs position x along the cylinder. Here x is the distance from the boundary of the cylinder converted to column index $x/a' \in [1, L]$ [cf. Fig. 1(a)].

ultrashort on the order of a single lattice spacing. But this ignores the fact that the bulk gap actually needs to physically close towards the open boundary. The lengthscale over which this occurs is, *a priori*, far from clear.

To gain further insight into the effect of the open boundary, we look more closely into correlations also with reference to the boundary for $YC6 \times 64$. The results are summarized in Fig. 7 where we take the ground state from the complex-valued DMRG simulation as in Fig. 6 after the last sweep. While $D^* = 8192$ already ensures visible convergence and established long-range chiral correlations, the variations in the data in Figs. 7(b)–7(d) around the system center $x \sim L/2 = 32$ need to be taken with a grain of salt, bearing in mind the residual variations in the data of the last sweep in Fig. 6(d) itself.

To start with, the bulk spin and charge correlations for YC6 remain extremely short-ranged, as seen Fig. 7(a). The correlation lengths are of about one lattice spacing, consistent with the YC4 data in Fig. 3. Given the slightly smaller $U = 9$ here, the correlation length for charge transfer is slightly increased, ($\xi_c = 0.81 \rightarrow 0.91$), yet the spin-spin correlation length is actually reduced ($\xi_s = 1.66 \rightarrow 1.20$), bringing the two correlation lengths closer to each other.

Now in order to analyze effects versus distance from the boundary, we compute chiral, spin, and charge correlations at fixed vertical distance $d_y = 3$ of site i relative to site

j (i.e., taken halfway around the cylinder) versus position $x/a' = 1, \dots, L$ along the cylinder, with the results shown in Figs. 7(b)–7(d), respectively. While superficially the data behave similarly, the magnitudes vary considerably, with the scale of values decreasing from chiral to spin to charge correlations, in agreement with the expected respective relevance in the low-energy regime. Furthermore, one notices that all data show pronounced oscillatory behavior close the boundary with a period of around four columns in YC6, i.e., $\lambda \simeq 4a'$. More importantly, the enveloping amplitude decays rather slowly into the bulk, taking about $\Delta x \sim 5\lambda$, i.e., 20 columns from the open boundary of the YC6 cylinder to diminish. Together with the right boundary, this suggests that in order for the effects of the open boundary to have significantly decayed to actually see bulk behavior in the system center, one needs a rather long cylinder with $L \gtrsim 10\lambda \sim 40$ columns. For shorter systems, the two boundaries can thus be expected to interfere with each other, which can be detrimental to the development of long-range chiral correlations, as observed, for example, for the shorter YC4 systems in Fig. 4.

IV. SUMMARY AND CONCLUSIONS

We show clear numerical evidence for an intermediate chiral spin-liquid phase on long yet finite-size YC4 and YC6 cylinders of the half-filled triangular lattice Hubbard model for sizable $U \in [U_{c1}, U_{c2}]$ based on exact large-scale DMRG simulations. This phase is surrounded by a metallic phase for $U < U_{c1}$ (or possibly a Luther-Emery liquid [16,53]), and a 120° magnetic insulating phase for $U > U_{c2}$. For YC4 we find $U_{c1} \simeq 9$ and $U_{c2} \simeq 10.75$, whereas for YC6, $U_{c2} \lesssim 10$. The intermediate spin-liquid phase has been debated intensely in recent literature, with contradicting conclusions on whether it represents a chiral spin liquid or not. Our results demonstrate that finite-size effects can drastically alter the conclusions. Here, the system length in DMRG simulation constitutes a key factor to identify the spontaneous TRS breaking in the CSL state.

In the effective spin model derived from the Hubbard model [7,28–30], the ring-exchange couplings have order t^4/U^3 . Previous study estimated the metal-insulator transition to occur at $U/t \simeq 5$ [10], leading to important ring-exchange couplings that can drive a spinon Fermi surface state [7]. However, DMRG studies find the Mott transition at $U/t \simeq 9$, which indicates the much weaker ring-exchange couplings and may explain why the spinon Fermi surface state is not found. Properly accounting for spin couplings in an effective spin model allows one to understand the emergence of the gapped CSL of Kalmeyer-Laughlin type [30].

A hand-waving argument on a possible origin of the CSL phase at the intermediate U may be taken from the phase diagram at finite temperature [52]. In the large U limit, TLU reduces to an effective Heisenberg spin model. Besides the long-wavelength soft modes at the K point corresponding to the 120° order, there exists additional rotonlike modes near the M point at higher energy [36]. The softening of the M -point rotonlike excitations, either by quantum fluctuations [54] or thermal fluctuations [36,43], seems to be accompanied by an emergent liquidlike phase with anomalously enhanced chiral fluctuations. Here the charge fluctuations also lead to a spin-

liquid phase with long-range chiral order and enhanced spin fluctuations at the M point, naturally implying the softening of the rotonlike excitations and spinon deconfinement in the transition with decreasing U . Therefore, it would be interesting and important to explore the spin dynamics of this Hubbard model in future study.

ACKNOWLEDGMENTS

We acknowledge the stimulating discussions with Olexei I. Motrunich and Hong-Hao Tu. W.L., Z.C., and S.-S.G. were supported by the National Natural Science Foundation of China Grants No. 11974036, No. 11834014, No. 11874078, No. 12074024, No. 11774018, No. 12222412, the Fundamental Research Funds for the Central Universities, and CAS Project for Young Scientists in Basic Research (Grant No. YSBR-057). D.N.S. was supported by National Science Foundation Grant No. PREM DMR-1828019. B.B.C. was also supported by the German Research foundation, DFG WE4819/3-1. B.B.C. and W.L. thank the High-performance Computing Center at ITP-CAS for the technical support and generous allocation of CPU time. A.W. was supported by the U.S. Department of Energy, Office of Science, Basic Energy Sciences, Materials Sciences and Engineering Division.

APPENDIX A: SYMMETRIC CONSTRUCTION OF A CHIRAL OPERATOR

With spin rotation SU(2) symmetry implemented, the spin operators need to be reorganized into an irreducible operator (irop), i.e., the spinor also schematically depicted in Fig. 8(a) [38],

$$\hat{S}^{q=1,m} \equiv \begin{pmatrix} \frac{-1}{\sqrt{2}} \hat{S}^+ \\ \hat{S}^z \\ \frac{1}{\sqrt{2}} \hat{S}^- \end{pmatrix}, \quad (\text{A1})$$

with the ladder operators $S^+ = (S^x + iS^y)$, $S^- = (S^x - iS^y)$. Here the components $\hat{S}^{1,+1}$, $\hat{S}^{1,0}$, and $\hat{S}^{1,-1}$ transform like an irreducible representation (irop) $|S; S_z\rangle$ with $S_z = +1, 0, -1$, respectively. For this, the relative sign on the first component is important. The spin operator always corresponds to the ad-

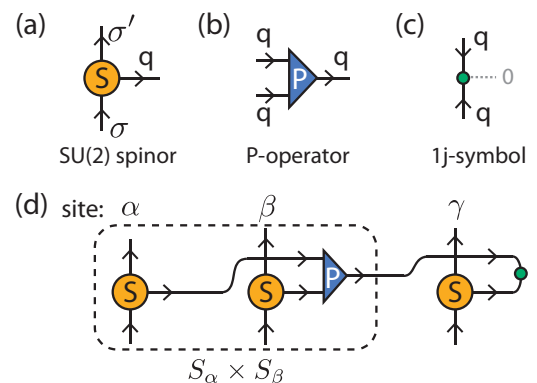


FIG. 8. Symmetric tensor representation of (a) SU(2) spinor S^q [Eq. (A1)], (b) P -operator, (c) the 1j-symbol, and (d) the scalar chirality operator order χ [cf. Eq. (A2b)].

joint representation, i.e., $S = 1$ for $SU(2)$. The normalization of the irop in Eq. (A1) is chosen such that $\hat{S}_i^\dagger \cdot \hat{S}_j$ corresponds to the standard Heisenberg interaction $\hat{S}_i \cdot \hat{S}_j$ where, nevertheless, when having Eq. (A1), the dagger on \hat{S}_i becomes important.

Next we can build the scalar chirality, which we expand as

$$\hat{\chi}_{ijk} = (\hat{\sigma}_i \times \hat{\sigma}_j) \cdot \hat{\sigma}_k \equiv 8(\hat{S}_i \times \hat{S}_j) \cdot \hat{S}_k \quad (\text{A2a})$$

$$= 4i(\hat{S}_i^+ \hat{S}_j^- \hat{S}_k^z + \hat{S}_i^z \hat{S}_j^+ \hat{S}_k^- + \hat{S}_i^- \hat{S}_j^z \hat{S}_k^+ - \text{H.c.}). \quad (\text{A2b})$$

Now while this may look somewhat tedious, in practice there is a simple transparent procedural way for dealing with it from a tensor network perspective with $SU(2)$ spin symmetry enabled. As is required for an observable, the chiral operator is a scalar operator with nonzero eigenvalues $\pm\sqrt{12}$. It combines three spin operators \hat{S} into a scalar operator $\hat{\chi}$. As depicted in Fig. 8(d), one needs to “tie together” the three $S = 1$ irop indices (horizontal leg for each S). This can be simply achieved by fusing two $S = 1$ multiplets (ingoing) into $S = 1$ (outgoing). From a symmetry perspective, this is also the only possible combination here. The result corresponds to a tensor \hat{P} that is proportional to the Clebsch-Gordan coefficient tensor (CGT) $C_{1,1}^1 \equiv (1, 1|1) \propto P$ [Fig. 8(b)]. With this, the chiral term can be compactly written as the nested contractions (denoted by $*$)

$$\hat{\chi}_{ijk} = (\hat{S}_i * (\hat{S}_j * \hat{P})) * \hat{S}_k^\dagger, \quad (\text{A3})$$

where the precise order of pairwise contractions by the brackets is irrelevant. Optionally, this expression can be further symmetrized. The direction of an arrow (leg) can be reversed based on a so-called “1j” symbol [39]. In the present case, this corresponds to the CGT $(1, 1|0) = \frac{1}{\sqrt{3}}U$ that fuses two $S = 1$ multiplets into a singlet. The index with the outgoing $S = 0$ is a singleton dimension and hence can be skipped. After proper normalization, this reduces to a unitary operator U [Fig. 8(c)]. Thus inserting $U^\dagger * U = 1$, having $U = U^\dagger$ here, and contracting one U onto the outgoing index of P , denoted as $P_A \equiv P * U$ [a green dot contracted onto a blue triangle in Fig. 8(d)], and the other U onto \hat{S}_k^\dagger (which effectively removes the dagger), the chiral term becomes [Fig. 8(d)]

$$\hat{\chi}_{ijk} = (\hat{S}_i * (\hat{S}_j * \hat{P}_A)) * \hat{S}_k, \quad (\text{A4})$$

now with all three spin operators \hat{S} on an equal symmetric footing. Here P_A is a completely antisymmetric tensor for its three indices, all of which are incoming now. As such, it corresponds to a Wigner $3j$ symbol, which in the present case precisely corresponds to the Levi-Civita tensor as it appears in the original definition of the chiral operator in Eq. (A2a), up to an overall purely imaginary normalization factor.

APPENDIX B: CONVERGENCE OF THE DMRG CALCULATION

In this Appendix, we show the computed entanglement entropy S_E and ground-state energy per site e_g versus bond dimension $1/D^*$. As can be seen below, the results shown in the main text for the intermediate chiral spin liquid (CSL) and large- U regimes are well-converged versus D^* . In practice, to

ensure convergence of the data, we ramp up the bond dimension D^* for sweep n in the uniform exponential manner, as described by $D_n^* = D_0^* a^n$. Here a is a parameter that controls the speed of increase of D^* from one sweep to the next, until the final bond dimension $D_{n_{\max}}^*$ is reached. We start with an initial bond dimension D_0^* during a random initialization in the global symmetry sector $(S, Q) = (0, 0)$, where S and Q denote the spin and charge quantum numbers, respectively. In this work, we use $D_0^* = 512$, $a = 2^{1/5}$, $D_{n_{\max}}^* = 8192$, and thus $n_{\max} = 20$ sweeps. This leads to well-converged results in most cases. In addition, we may slow down the ramping of D^* by actually performing up to five sweeps for a given “stage” n , before moving on to the next stage $n + 1$ with increased bond dimension D_{n+1}^* , e.g., seen as vertical stacking of data points in Fig. 9.

In the left panels of Fig. 9, we show particular specifics of the block-entanglement entropy simulations as we ramp up the number of multiplets D^* in our DMRG simulations. We show both the maximum values of entanglement entropy S_E (labeled by “Max”) and the ones cutting at the center bond of the system (labeled by “Mid”). In Fig. 9(a), for $U = 8$, we can see the fast growth of entanglement entropy S_E , expected in a metallic state that is extremely challenging for the DMRG calculation, even though overall convergence, e.g., of the ground-state energy, already appears systematic. For the CSL phase at $U = 10$ [panels (c),(g)] and the magnetically ordered phase at $U = 12$ [panel (e)], S_E results are well converged versus $1/D^*$.

In the right panels of Fig. 9, we check the convergence of the ground-state energy e_g . We linearly extrapolate it towards $1/D^* \rightarrow 0$ based on the last three data points (red line in the insets). We use the extrapolated value $e_g^0 \equiv \lim_{1/D^* \rightarrow 0} e_g(D^*)$ to estimate the “error” of finite-bond-dimension energy as the difference $\epsilon_e \equiv e_g(D^*) - e_g^0$, as shown in the main right panels in Fig. 9. From these we see that, within their respective system size, at $L = 18$ the energies are converged to $\epsilon_e \sim 10^{-4}$ for $U = 8$ and to $\epsilon_e \sim 10^{-5}$ for $U = 10, 12$; and at $L = 64$, the energies are converged to $\epsilon_e \sim 10^{-4}$ for $U = 10$.

Overall, convergence is not always smooth with increasing bond dimension D^* . For example, there may be excitations in the system due to the arbitrary initialization of the wave function for small D^* which, nevertheless, get ironed out early on. Certain low-energy excitation as well as edge modes can be dealt with over longer distances only once a sufficient accuracy, i.e., sufficiently large D^* , has been reached, which then may lead to a rather sharp drop or increase in the maximal block entanglement across the entire system, as well as a rapid drop of energy, as observed for intermediate and also larger D^* .

On a physical level, a certain choice of D^* permits a certain energy resolution, as evident from the analysis of the right panels of Fig. 9. This gives insights into the energy scales of the system under consideration. Consider, for example, the bottom panels of Fig. 9 for the chiral intermediated state at $U = 10$ for $L = 64$. There the chirality of the ground state only emerges for $D^* \gtrsim 2500$ ($1/D^* \lesssim 4 \times 10^{-4}$), which leads to a sharp rise in the entanglement entropy [Fig. 9(g)]. This by itself already suggests a significant change in the underlying DMRG wave function, e.g., as also seen in the convergence of the chiral long-range correlation in Fig. 4(a) of the main

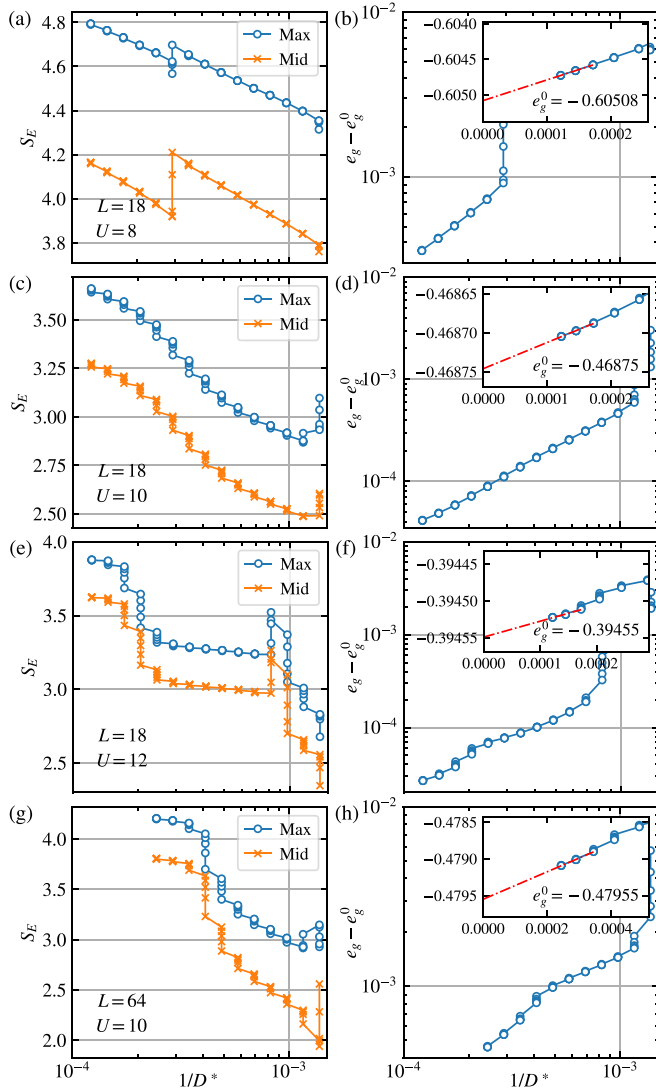


FIG. 9. Entanglement entropy S_E (left panels) and ground-state energy (right panels) vs $1/D^*$ for YC4 for (a),(b) $U = 8$; (c),(d) $U = 10$; (e),(f) $U = 12$ at $L = 18$; and (g),(h) $U = 10$ at $L = 64$. Entanglement entropy S_E labeled “Max” are the maximal entanglement among all bonds throughout the system, while the “Mid” ones are values measured at the center of the systems. The linear extrapolations with $1/D^*$ are shown in the inset of all right panels (b),(d),(f),(h). Although the calculations are very challenging in the metallic phase with $U = 8$, the data have reached very good convergence for $U = 10$ and 12.

text. Indeed, the systematic degeneracies in the entanglement spectra also only emerge once the sufficiently large $D^* \gtrsim 2500$ is reached in the present case. Simultaneous with a strong rise in the entanglement entropy in Fig. 9(g), one also observes a kink in the convergence of the ground-state energy [Fig. 9(h)].

This suggests that for the chiral state to be seen in the DMRG simulations, one needs an energy resolution such as that found at the kink, that is, $\Delta e_\chi \cong e_g - e_g^0 \simeq 10^{-3}$. If one were to interpret this to reflect an actual energy gap below which the DMRG convergence is accelerated, the corresponding estimate would be $\Delta_\chi \cong LW \Delta e_\chi \simeq 0.25$ and thus sizable. Increasing the ground-state energy of the $L = 64$ system by

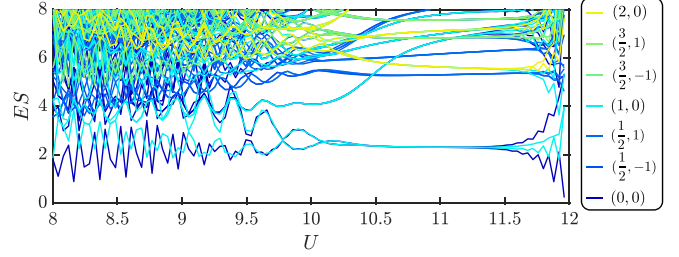


FIG. 10. Entanglement spectrum (ES) along the system and in between full columns of a DMRG scan along a YC4 \times 100 cylinder. For this we tune $U \in [8, 12]$ linearly along the cylinder. We keep the bond dimensions up to $D^* = 5793$ ($D \lesssim 17053$). The lines are color-coded according to their symmetry sector (S, Q) as indicated.

adding Δe_χ , it still has a significantly lower energy than the $L = 18$ system, given that $\Delta e_g^0 = e_g^0(L = 18) - e_g^0(L = 64) \sim 0.011$. Conversely then, a nonchiral state may be seen if the energy of a given (eigen)state is higher by Δ_χ above the ground state for a given width $W = 4$ system, either due to insufficient D^* or due to finite-length effects. The latter is demonstrated by comparison to the same $U = 10$ Hamiltonian, yet for the significantly shorter $L = 18$ in Figs. 9(c) and 9(d). From the above estimates, the finite size correction for this smaller system size is significantly larger than Δ_χ , and so we do not yet see a chiral signature in its converged ground state [see also Fig. 13(a)]. Therefore, also the entanglement profile in Fig. 9(c) evolves much more smoothly as compared to Fig. 9(g), and the convergence of the ground-state energy in Fig. 9(d) also shows no kink.

APPENDIX C: DMRG SCAN OF THE CYLINDER WITH SMOOTHLY CHANGING U

To study the phase diagram of the model, we also performed a linear DMRG scan [55] for a YC4 \times 100 system with the varying U for different columns i as $U_i = U_1 + \frac{i-1}{L-1}(U_L - U_1)$. Here, we set $U_1 = 8$ for the first column and $U_L = 12$ for the last one. The results are shown in Fig. 10, where we compute and collect the entanglement spectra for each cut between the columns i and $i + 1$. Since each column i corresponds to a unique U_i , the ES “flows” as U changes along the cylinder.

In the present YC4 system, three possible phases can be discerned in the entanglement spectrum, separated by the two critical points at $U_{c1} \simeq 9.5$ and $U_{c2} \simeq 10.5$. The ES is nondegenerate in the small- U ($U < 9.5$) phase, while it approaches fourfold and eightfold degeneracy in the intermediate- U ($9.5 < U < 10.5$) and large- U ($U > 10.5$) regime (two- and four-multiplet degeneracy, respectively). When approaching the open right boundary of the cylinder at $U = 12$, the degeneracy starts to split again. This is consistent with the splitting in the ES between the $S = 0$ and 1 multiplets already discussed with Figs. 4(c) and 4(d) in main text.

APPENDIX D: DESTRUCTION OF THE FERMI SURFACE

In Fig. 11, we show the electron density in momentum space n_q on the YC4 \times 18 system. The distribution n_q of the free fermion system at $U = 0$ in the thermodynamic limit

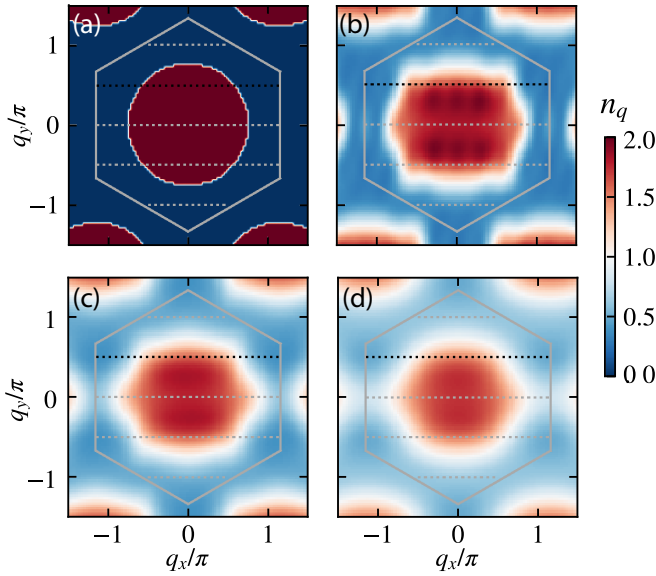


FIG. 11. Electron density in the momentum space n_q on the $YC4 \times 18$ systems with (a) $U = 0$, (b) $U = 8$, (c) $U = 9$, and (d) $U = 10$. Gray hexagons represent the boundary of first Brillouin zone, and the horizontal dotted lines represent the allowed momenta q_y for the YC4 cylinder.

is also included in Fig. 11(a) as a reference, which shows a perfect Fermi surface. In Figs. 11(b)–11(d), the calculated n_q exhibits a recognizable Fermi surface at $U = 8$. With further growing U , the Fermi surface gets significantly blurred at $U = 9$ and 10, characterizing a metal-insulator transition with a destructed Fermi surface.

APPENDIX E: CHARGE GAP

In this Appendix, we directly calculate the charge (single-particle excitation) gap,

$$\Delta_C = \frac{1}{2} [E(\frac{1}{2}, +1) + E(\frac{1}{2}, -1) - 2E(0, 0)],$$

where $E(S, Q)$ denotes the lowest eigenenergy with total spin S , and charge Q is taken as the number of particles relative to the half-filling. For the ground state we have $S = Q = 0$. As shown in Fig. 12 for $U = 10$, Δ_C decreases with system

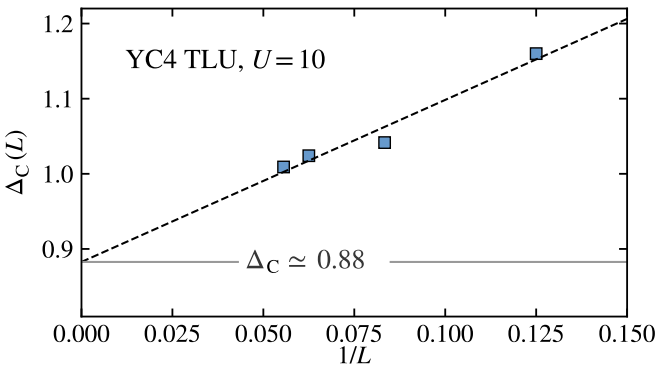


FIG. 12. Charge gap Δ_C calculated on the YC4 cylinders with different lengths $L = 8, 12, 16, 18$. The linearly extrapolated value with $L \rightarrow \infty$ is $\Delta_C \simeq 0.88$.

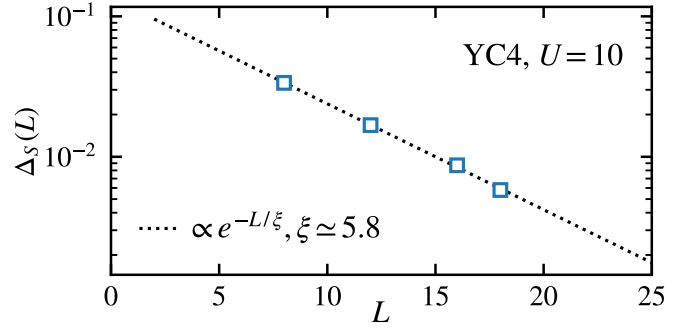


FIG. 13. Energy difference Δ_S between the total spin-0 and total spin-1 sectors. We calculate the YC4 cylinders with system length $L = 8, 12, 16, 18$. This shows an exponential decay with $\xi \simeq 5.8$ with increasing L as indicated.

length L , and the linear extrapolation over $1/L$ results in a large nonzero gap $\Delta_C \simeq 0.88$. This confirms that the spin liquid resides in the Mott insulating phase.

APPENDIX F: IDENTIFICATION OF EDGE SPINONS FROM SPIN EXCITATION

In the CSL phase, we have found the obtained ground state (on the YC4 cylinder) in the semion topological sector, with a spin-1/2 spinon on each open boundary. Therefore, we expect a fourfold ground-state degeneracy ($S = 0 \oplus 1$) for sufficiently long cylinders. This may be seen analogous to the Haldane phase of the open $S = 1$ spin chain, where also spin-1/2 edge modes are weakly coupled. Thus, the energy difference between the total spin-0 and spin-1 sectors is expected to decay exponentially with growing system size [56].

Here, we use a similar strategy to identify the edge spinons in the semion sector of the CSL state. We show the energy difference Δ_S between the total spin-0 and spin-1 sectors with growing system length in Fig. 13. Clearly, Δ_S is very small and indeed decays exponentially with L . Since the spin triplet excitation is gapped in the bulk (cf. Fig. 3 in THE main text), this vanishing energy difference must be ascribed to the edge spinon modes in the semion sector of the CSL.

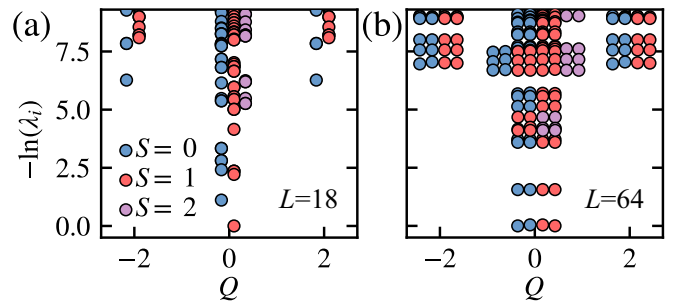


FIG. 14. Entanglement spectrum calculated at the center of YC4 systems with (a) $L = 18$ and (b) $L = 64$ [cf. Fig. 4(c) in the main text], grouped by charge sectors (showing even Q only), with spin labels color-coded as specified in the legend.

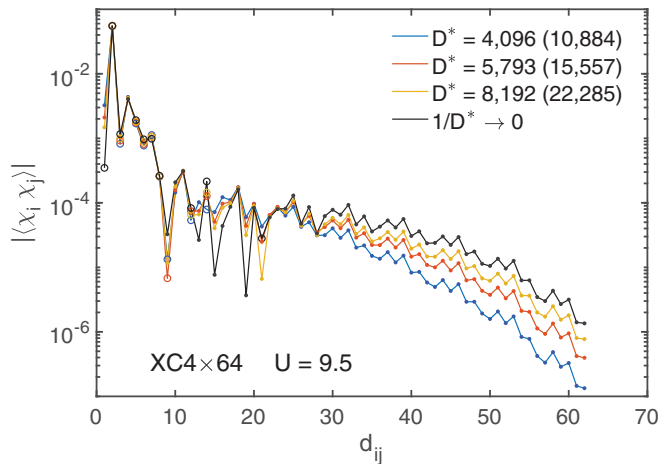


FIG. 15. Chiral correlations calculated in a $U = 9.5$ $XC4 \times 64$ system with bond dimensions $D^* = 4096, 5793, 8192$ show no long-range correlations. The black line depicts the results of linear extrapolation $1/D^* \rightarrow 0$ from the above bond dimensions. Here, the filled symbol indicated the positive sign of chiral correlation, and otherwise the sign is negative.

APPENDIX G: FINITE-SIZE EFFECT OF TRS BREAKING DETECTION

To further emphasize the absence OF long-range chiral correlation on short systems, we also contrast the ES for $L = 18-64$ in the main paper. As seen in Fig. 14, $L = 18$ is still clearly qualitatively different. An obvious difference from the ES for $L = 64$ [Fig. 14(b)] is the complete absence of degeneracies, which, in particular, demonstrates that the two low-lying real wave functions that respect TRS are still split

by a relatively large gap due to finite-size effects. Therefore, simulations on such short systems may lead to the premature conclusion of no chiral order. However, with growing system length L , this gap decreases and eventually becomes negligible. This then allows DMRG calculation to obtain the minimal entangled state with spontaneous TRS breaking [57].

APPENDIX H: CHIRAL CORRELATION ON AN XC4 SYSTEM

In this Appendix, we show the chiral correlations $\langle \chi_i \chi_j \rangle$ between two triangles labeled i and j with distance $d = |i - j|$, in $XC4 \times 64$ systems for the case of $U = 9.5$. As shown in Fig. 15, with a bond dimension up to $D^* = 8192$ $SU(2)$ multiplets (corresponding to $D > 22000$ individual states), chiral correlations are strongly suppressed. We further perform a linear $1/D^* \rightarrow 0$ extrapolation from the correlation data of the largest three bond dimensions $D^* = 4096, 5793, 8192$, and still see no sign of long-range chiral correlation. Hence $XC4$ behaves very differently from $YC4$ or $YC6$, where for cylinders of the same length already robust long-range chiral correlations were observed, having $\chi^2 = 0.128$ for $YC4$ at $D^* = 4096$ (Fig. 4), or $\chi^2 \approx 0.25$ for $YC6$ at $D^* \gtrsim 8192$ (Fig. 6). Here for $XC4$, the chiral correlations drop rapidly over short distances $d_{ij} < 10$. However, they appear to gain weak support for $d_{ij} > 10$ around the much smaller value $\chi^2 \sim 10^{-4}$. While the long-distance correlations still gain strength with increasing D^* , nevertheless the chiral correlations do show (weak) decay with distance, even within the numerically converged range $d_{ij} \lesssim 25$. In this sense, we see no clear support for long-range chiral correlation in $XC4$ cylinders.

- [1] P. Anderson, Resonating valence bonds: A new kind of insulator?, *Mater. Res. Bull.* **8**, 153 (1973).
- [2] P. W. Anderson, The resonating valence bond state in La_2CuO_4 and superconductivity, *Science* **235**, 1196 (1987).
- [3] P. A. Lee, N. Nagaosa, and X.-G. Wen, Doping a Mott insulator: Physics of high-temperature superconductivity, *Rev. Mod. Phys.* **78**, 17 (2006).
- [4] L. Balents, Spin liquids in frustrated magnets, *Nature (London)* **464**, 199 (2010).
- [5] L. Savary and L. Balents, Quantum spin liquids: A review, *Rep. Prog. Phys.* **80**, 016502 (2017).
- [6] Y. Zhou, K. Kanoda, and T.-K. Ng, Quantum spin liquid states, *Rev. Mod. Phys.* **89**, 025003 (2017).
- [7] O. I. Motrunich, Variational study of triangular lattice spin-1/2 model with ring exchanges and spin liquid state in $\kappa-(ET)_2Cu_2(CN)_3$, *Phys. Rev. B* **72**, 045105 (2005).
- [8] S.-S. Lee and P. A. Lee, $U(1)$ Gauge Theory of the Hubbard Model: Spin Liquid States and Possible Application to $\kappa-(BEDT-TTF)_2Cu_2(CN)_3$, *Phys. Rev. Lett.* **95**, 036403 (2005).
- [9] S. Sorella, Y. Otsuka, and S. Yunoki, Absence of a spin liquid phase in the Hubbard model on the honeycomb lattice, *Sci. Rep.* **2**, 992 (2012).
- [10] H. Morita, S. Watanabe, and M. Imada, Nonmagnetic insulating states near the mott transitions on lattices with geometrical frustration and implications for $\kappa-(ET)_2Cu_2(CN)_3$, *J. Phys. Soc. Jpn.* **71**, 2109 (2002).
- [11] T. Koretsune, Y. Motome, and A. Furusaki, Exact diagonalization study of mott transition in the hubbard model on an anisotropic triangular lattice, *J. Phys. Soc. Jpn.* **76**, 074719 (2007).
- [12] P. Sahebsara and D. Sénéchal, Hubbard Model on the Triangular Lattice: Spiral Order and Spin Liquid, *Phys. Rev. Lett.* **100**, 136402 (2008).
- [13] T. Yoshioka, A. Koga, and N. Kawakami, Quantum Phase Transitions in the Hubbard Model on a Triangular Lattice, *Phys. Rev. Lett.* **103**, 036401 (2009).
- [14] T. Shirakawa, T. Tohyama, J. Kokalj, S. Sota, and S. Yunoki, Ground-state phase diagram of the triangular lattice Hubbard model by the density-matrix renormalization group method, *Phys. Rev. B* **96**, 205130 (2017).
- [15] A. Szasz, J. Motruk, M. P. Zaletel, and J. E. Moore, Chiral Spin Liquid Phase of the Triangular Lattice Hubbard Model: A Density Matrix Renormalization Group Study, *Phys. Rev. X* **10**, 021042 (2020).
- [16] A. Szasz and J. Motruk, Phase diagram of the anisotropic triangular lattice Hubbard model, *Phys. Rev. B* **103**, 235132 (2021).

- [17] Y. Shimizu, K. Miyagawa, K. Kanoda, M. Maesato, and G. Saito, Spin Liquid State in an Organic Mott Insulator with a Triangular Lattice, *Phys. Rev. Lett.* **91**, 107001 (2003).
- [18] Y. Kurosaki, Y. Shimizu, K. Miyagawa, K. Kanoda, and G. Saito, Mott Transition from a Spin Liquid to a Fermi Liquid in the Spin-frustrated Organic Conductor κ -(ET)₂Cu₂(CN)₃, *Phys. Rev. Lett.* **95**, 177001 (2005).
- [19] S. Yamashita, Y. Nakazawa, M. Oguni, Y. Oshima, H. Nojiri, Y. Shimizu, K. Miyagawa, and K. Kanoda, Thermodynamic properties of a spin-1/2 spin-liquid state in a κ -type organic salt, *Nat. Phys.* **4**, 459 (2008).
- [20] T. Isono, H. Kamo, A. Ueda, K. Takahashi, M. Kimata, H. Tajima, S. Tsuchiya, T. Terashima, S. Uji, and H. Mori, Gapless Quantum Spin Liquid in an Organic Spin-1/2 Triangular-lattice κ -H₃(Cat-EDT-TTF)₂, *Phys. Rev. Lett.* **112**, 177201 (2014).
- [21] T. Isono, T. Terashima, K. Miyagawa, K. Kanoda, and S. Uji, Quantum criticality in an organic spin-liquid insulator κ -(BEDT - TTF)₂Cu₂(CN)₃, *Nat. Commun.* **7**, 13494 (2016).
- [22] B. Miksch, A. Pustogow, M. J. Rahim, A. A. Bardin, K. Kanoda, J. A. Schlueter, R. Hübner, M. Scheffler, and M. Dressel, Gapped magnetic ground state in quantum spin liquid candidate κ -(BEDT - TTF)₂Cu₂(CN)₃, *Science* **372**, 276 (2021).
- [23] M. Yamashita, N. Nakata, Y. Senshu, M. Nagata, H. M. Yamamoto, R. Kato, T. Shibauchi, and Y. Matsuda, Highly Mobile Gapless Excitations in a Two-Dimensional Candidate Quantum Spin Liquid, *Science* **328**, 1246 (2010).
- [24] S. Yamashita, T. Yamamoto, Y. Nakazawa, M. Tamura, and R. Kato, Gapless spin liquid of an organic triangular compound evidenced by thermodynamic measurements, *Nat. Commun.* **2**, 275 (2011).
- [25] P. Bourgeois-Hope, F. Laliberté, E. Lefrançois, G. Grissonnanche, S. R. de Cotret, R. Gordon, S. Kitou, H. Sawa, H. Cui, R. Kato, L. Taillefer, and N. Doiron-Leyraud, Thermal conductivity of the quantum spin liquid candidate EtMe₃Sb[Pd(dmit)₂]₂: No evidence of mobile gapless excitations, *Phys. Rev. X* **9**, 041051 (2019).
- [26] J. M. Ni, B. L. Pan, B. Q. Song, Y. Y. Huang, J. Y. Zeng, Y. J. Yu, E. J. Cheng, L. S. Wang, D. Z. Dai, R. Kato, and S. Y. Li, Absence of Magnetic Thermal Conductivity in the Quantum Spin Liquid Candidate EtMe₃Sb[Pd(dmit)₂]₂, *Phys. Rev. Lett.* **123**, 247204 (2019).
- [27] D. F. Schroeter, E. Kapit, R. Thomale, and M. Greiter, Spin Hamiltonian for which the Chiral Spin Liquid is the Exact Ground State, *Phys. Rev. Lett.* **99**, 097202 (2007).
- [28] D. N. Sheng, O. I. Motrunich, and M. P. A. Fisher, Spin Bose-metal phase in a spin- $\frac{1}{2}$ model with ring exchange on a two-leg triangular strip, *Phys. Rev. B* **79**, 205112 (2009).
- [29] H.-Y. Yang, A. M. Läuchli, F. Mila, and K. P. Schmidt, Effective Spin Model for the Spin-Liquid Phase of the Hubbard Model on the Triangular Lattice, *Phys. Rev. Lett.* **105**, 267204 (2010).
- [30] T. Cookmeyer, J. Motruk, and J. E. Moore, Four-Spin Terms and the Origin of the Chiral Spin Liquid in Mott Insulators on the Triangular Lattice, *Phys. Rev. Lett.* **127**, 087201 (2021).
- [31] M. S. Block, D. N. Sheng, O. I. Motrunich, and M. P. A. Fisher, Spin Bose-metal and Valence Bond Solid Phases in a Spin-1/2 Model with Ring Exchanges on a Four-leg Triangular Ladder, *Phys. Rev. Lett.* **106**, 157202 (2011).
- [32] V. Kalmeyer and R. B. Laughlin, Equivalence of the Resonating-valence-bond and Fractional Quantum Hall States, *Phys. Rev. Lett.* **59**, 2095 (1987).
- [33] B. Bauer, L. Cincio, B. Keller, M. Dolfi, G. Vidal, S. Trebst, and A. Ludwig, Chiral spin liquid and emergent anyons in a kagome lattice mott insulator, *Nat. Commun.* **5**, 5137 (2014).
- [34] W.-J. Hu, S.-S. Gong, W. Zhu, and D. N. Sheng, Competing spin-liquid states in the spin- $\frac{1}{2}$ Heisenberg model on the triangular lattice, *Phys. Rev. B* **92**, 140403(R) (2015).
- [35] S.-S. Gong, W. Zheng, M. Lee, Y.-M. Lu, and D. N. Sheng, Chiral spin liquid with spinon Fermi surfaces in the spin- $\frac{1}{2}$ triangular Heisenberg model, *Phys. Rev. B* **100**, 241111(R) (2019).
- [36] L. Chen, D.-W. Qu, H. Li, B.-B. Chen, S.-S. Gong, J. von Delft, A. Weichselbaum, and W. Li, Two-temperature scales in the triangular-lattice Heisenberg antiferromagnet, *Phys. Rev. B* **99**, 140404(R) (2019).
- [37] S. R. White, Density Matrix Formulation for Quantum Renormalization Groups, *Phys. Rev. Lett.* **69**, 2863 (1992).
- [38] A. Weichselbaum, Non-abelian symmetries in tensor networks: A quantum symmetry space approach, *Ann. Phys.* **327**, 2972 (2012).
- [39] A. Weichselbaum, X-symbols for non-abelian symmetries in tensor networks, *Phys. Rev. Res.* **2**, 023385 (2020).
- [40] C. L. Henley, Ordering Due to Disorder in a Frustrated Vector Antiferromagnet, *Phys. Rev. Lett.* **62**, 2056 (1989).
- [41] S. R. White and A. L. Chernyshev, Néel Order in Square and Triangular Lattice Heisenberg Models, *Phys. Rev. Lett.* **99**, 127004 (2007).
- [42] A. Weichselbaum and S. R. White, Incommensurate correlations in the anisotropic triangular Heisenberg lattice, *Phys. Rev. B* **84**, 245130 (2011).
- [43] B.-B. Chen, L. Chen, Z. Chen, W. Li, and A. Weichselbaum, Exponential Thermal Tensor Network Approach for Quantum Lattice Models, *Phys. Rev. X* **8**, 031082 (2018).
- [44] Although the Brillouin zone of the YC4 system does not contain the K point, we can still compute the Fourier transform of spin correlations at this momentum, as a proper approximation.
- [45] M. Laubach, R. Thomale, C. Platt, W. Hanke, and G. Li, Phase diagram of the Hubbard model on the anisotropic triangular lattice, *Phys. Rev. B* **91**, 245125 (2015).
- [46] P. Calabrese and J. Cardy, Entanglement entropy and quantum field theory, *J. Stat. Mech.* (2004) P06002.
- [47] W. Li, A. Weichselbaum, and J. von Delft, Identifying symmetry-protected topological order by entanglement entropy, *Phys. Rev. B* **88**, 245121 (2013).
- [48] Y.-H. Wu, L. Wang, and H.-H. Tu, Tensor Network Representations of Parton Wave Functions, *Phys. Rev. Lett.* **124**, 246401 (2020).
- [49] P. Francesco, P. Mathieu, and D. Sénéchal, *Conformal Field Theory* (Springer Science & Business Media, 2012).
- [50] H. Li and F. D. M. Haldane, Entanglement Spectrum as a Generalization of Entanglement Entropy: Identification of Topological Order in Non-Abelian Fractional Quantum Hall Effect States, *Phys. Rev. Lett.* **101**, 010504 (2008).

- [51] L. F. Tocchio, A. Montorsi, and F. Becca, Hubbard model on triangular N -leg cylinders: Chiral and nonchiral spin liquids, *Phys. Rev. Res.* **3**, 043082 (2021).
- [52] A. Wietek, R. Rossi, F. Šimkovic, M. Klett, P. Hansmann, M. Ferrero, E. M. Stoudenmire, T. Schäfer, and A. Georges, Mott Insulating States with Competing Orders in the Triangular Lattice Hubbard Model, *Phys. Rev. X* **11**, 041013 (2021).
- [53] Y. Gannot, Y.-F. Jiang, and S. A. Kivelson, Hubbard ladders at small U revisited, *Phys. Rev. B* **102**, 115136 (2020).
- [54] F. Ferrari and F. Becca, Dynamical Structure Factor of the J_1 - J_2 Heisenberg Model on the Triangular Lattice: Magnons, Spinons, and Gauge Fields, *Phys. Rev. X* **9**, 031026 (2019).
- [55] Z. Zhu and S. R. White, Spin liquid phase of the $s = \frac{1}{2}J_1 - J_2$ Heisenberg model on the triangular lattice, *Phys. Rev. B* **92**, 041105(R) (2015).
- [56] T. Kennedy, Exact diagonalisations of open spin-1 chains, *J. Phys.: Condens. Matter* **2**, 5737 (1990).
- [57] H.-C. Jiang, Z. Wang, and L. Balents, Identifying topological order by entanglement entropy, *Nat. Phys.* **8**, 902 (2012).